Possible Wigner states in CrI$_3$ heterostructures with graphene: A tight-binding model perspective

Igor Rozhansky [*] and Vladimir Fal'ko

National Graphene Institute, University of Manchester, Manchester M13 9PL, United Kingdom

In this study, we present an effective tight-binding model for an accurate description of the lowest energy quadruplet of a conduction band in a ferromagnetic CrX_3 monolayer, tuned to the complementary *ab initio* density functional theory simulations. This model, based on a minimum number of chromium orbitals, captures a distinctively flat dispersion in those bands but requires taking into account hoppings beyond nearest neighbors, revealing ligand-mediated electron pathways connecting remote chromium sites. Doping of states in the lowest conduction band of CrX_3 requires charge transfer, which, according to recent studies [Tenasini *et al.*, Nano Lett. **22**, 6760 (2022); Tseng *et al.*, Nano Lett. **22**, 8495 (2022); Cardoso *et al.*, Phys. Rev. B **108**, 184423 (2023)], can occur in graphene(G)/CrX_3 heterostructures. Here, we use the detailed description of the lowest conduction band in CrI$_3$ to show that G/CrI$_3$/G and G/CrI$_3$ are type-II heterostructures where light holes in graphene would coexist with heavy electrons in the magnetic layer, where the latter can be characterized by Wigner-Seitz radius $r_s \sim 25-35$ (as estimated for hBN-encapsulated structures).

I. INTRODUCTION

Chromium trihalides (CrX_3, where $X = $ Cl, Br, or I) form a fascinating family of van der Waals materials, celebrated for their versatile magnetic properties [1–9]. Over the recent years a broad range of studies of these magnetic insulators has been performed on both bulk materials and atomically thin films produced by mechanical exfoliation [10–24]. While the main focus of those studies was on magnetic properties of CrX_3 compounds and their dependence on the number of layers [11,25–31], various CrX_3 films were also implemented in heterostructures with other two-dimensional (2D) materials, like graphene, with a view to proximitize ferromagnetic exchange [32–35]. A by-product of such studies was an observation of a substantial charge transfer between graphene and CrX_3 reported by several groups [10,32], attributed to electrons filling narrow conduction bands of CrX_3 [16,18], rather than impurity states inside its bandgap.

The above-mentioned observation opens an interesting avenue toward creating a 2D material that would combine both highly mobile holes in graphene with strongly correlated heavy electrons in CrX_3. Such a system is sketched in Fig. 1: a trilayer assembled from two graphenes with an embedded CrX_3 monolayer, where the transfer of electrons is hosted by the lowest spin-polarized conduction band of CrX_3. To describe this band (together with three more bands that belong to a quadruplet traced [16,18,25,37–39] to d orbitals of chromium), we develop an effective tight-binding (TB) model based on a minimal number of Cr orbitals and parametrized by

comparison with density-functional theory (DFT) calculations for CrI$_3$. This gives us access to the accurate description of the conduction band edge across the entire Brillouin zone, hence, obtaining a description of doping features of G/CrI$_3$/G stacks, and a possibility to estimate the Wigner-Seitz radius for the heavy electrons.

II. TIGHT-BINDING MODEL FOR CrX_3 MONOLAYER

In the crystal structure [40–43] of CrX_3, illustrated in Fig. 2(a), metal ions form a honeycomb middle-sublayer lattice, bonded by halogen atoms in the outer sublayers. Following an analogy with graphene, we divide Cr sites into A and B sublattices. Similarly to graphene, the crystal lattice has inversion symmetry with respect to the centers of the honeycombs and $y \rightarrow -y$ mirror symmetry; however, it lacks mirror
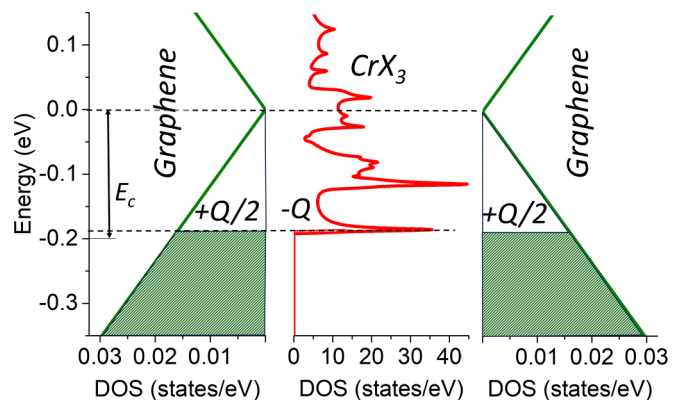

FIG. 1. Charge transfer in G/CrX_3/G trilayer. The density of states for graphene (left and right) and CrX_3 (center) is shown with an offset E_c ($E_c = 0.2$ eV for CrI$_3$ as in Ref. [36]), which leads to the transfer of electrons from graphene to the lowest empty band of the d-orbitals-based quadruplet in CrX_3 highlighted in Fig. 2. Painted areas indicate occupied states.

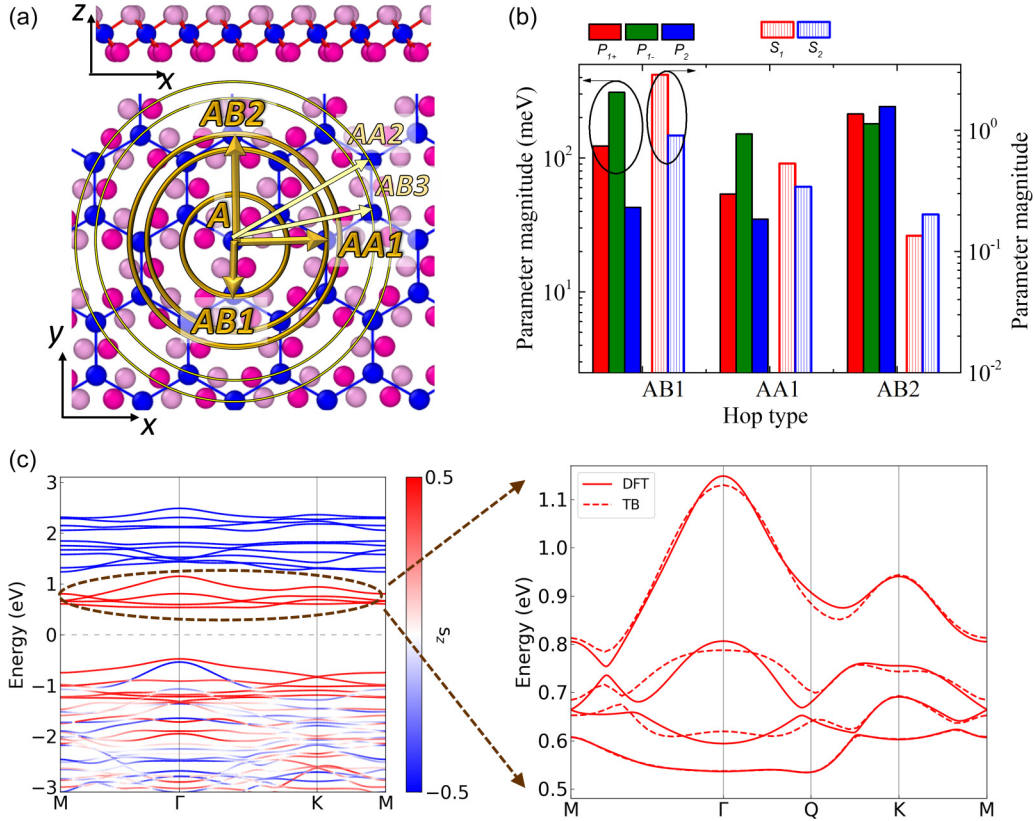*Contact author: igor.rozhanskiy@manchester.ac.uk

FIG. 2. Parametrization of the tight-binding model of CrI$_3$ using its DFT computed band structure. (a) Lattice structure of CrX_3 monolayers (X = I, Cl, Br). Cr ions (blue circles) form a honeycomb lattice; lighter and darker pink circles show halogen positions in upper and lower sublayers. Yellow lines show coordination circles labeled with a hop type. (b) The magnitudes of parameters used in the parametrization. (c) Left: DFT-calculated band structure of CrI$_3$ (with SOC taken into account) with color-coding reflecting spin polarization of the bands. The bottom of the conduction band is dominated by a quadruplet formed of chromium orbitals in Eq. (1) implemented in the tight-binding model (3). Right: the result of tight-binding model (3) parametrization (Table I), which accounts for Cr-Cr hoppings up to third neighbor, compared with the DFT data.

symmetry with respect to the horizontal plane and $x \rightarrow -x$ mirror symmetry, due to three out of six nearest halogen atoms lifted into the top sublayer and the other three pushed down to the bottom sublayers. This makes the symmetry group of the crystal D_{3d}.

Recent *ab initio* DFT modeling of various CrX_3 monolayers has indicated that wavefunctions of a quadruplet of the lowest spin-polarized conduction bands are dominated by d orbitals of chromium atoms [16,18,25,37–39]. Therefore, in the TB model described below, we implement a basis of mixed orbitals that would belong to the $e_{g\sigma}$ doublet at each Cr site, where, in addition to d orbitals we include a permitted admixture of p orbitals as a way to mimic the hybridization with halogen atoms:

$$\psi_{A1} = \alpha Y_2^2 - \beta(\zeta Y_2^{-1} + \eta Y_1^{-1});$$
$$\psi_{A2} = \alpha Y_2^{-2} + \beta(\zeta Y_2^1 - \eta Y_1^1);$$
$$\psi_{B1} = \alpha Y_2^2 - \beta(\zeta Y_2^{-1} - \eta Y_1^{-1});$$
$$\psi_{B2} = \alpha Y_2^{-2} + \beta(\zeta Y_2^1 + \eta Y_1^1);$$
$$\alpha^2 + \beta^2 = 1; \quad \zeta^2 + \eta^2 = 1. \qquad (1)$$

Here, Y_l^m are spherical harmonics; α, β are on-site mixing parameters for $m = 2(-2)$ and $m = -1(1)$ angular harmonics; ζ, η describe the mixing between $l = 1$ and $l = 2$ harmonics with $|m| = 1$; ψ_{Aj} and ψ_{Bj} are associated with two orbitals ($j = 1, 2$) at A and B sites, respectively. The spatial distribution of the density of such basis states reflects the threefold rotational symmetry of the CrX_3 lattice. This basis gives $E \times E$ reducible representation of the D_{3d} point group.

We use this basis as a minimal set to formulate an effective TB model describing the conduction band quadruplet highlighted in the CrI$_3$ monolayer band-structure displayed in Fig. 2(b). This band structure was obtained by DFT modeling of the ferromagnetic CrI$_3$ monolayer (magnetized along z axis) using the DFT + U + J scheme within the Quantum-Espresso *ab initio* package [44,45] with fully relativistic pseudopotentials [thus, taking the full account of spin-orbit coupling (SOC)] and the Perdew-Burke-Ernzerhof (PBE) approximation for the exchange-correlation functional [46]. For U and J, we take $U = 1.5$ eV and $J = 0.5$ eV [19]. The effect of SOC on the band structure both in DFT and TB calculations is additionally shown in the Supplemental Material [47].

For the plane-wave version of the TB model we use Bloch functions and an effective Schrödinger equation,

$$\chi_{Aj,\mathbf{q}} \cdot (\mathbf{r}) = \sum_{\mathbf{R}} \frac{e^{i\mathbf{q}\cdot\mathbf{R}}}{\sqrt{N}} \psi_{Aj}(\mathbf{r}-\mathbf{R}); \quad \chi_{Bj,\mathbf{q}}(\mathbf{r}) = \sum_{\mathbf{R}} \frac{e^{i\mathbf{q}\cdot\mathbf{R}}}{\sqrt{N}} \psi_{Bj}(\mathbf{r}-\mathbf{R});$$

$$(\mathcal{H}_{\mathbf{q}} - E_{\mathbf{k}}\mathcal{S}_{\mathbf{q}})\begin{pmatrix} A_1 \\ A_2 \\ B_1 \\ B_2 \end{pmatrix}_k = 0, \tag{2}$$

where $\mathbf{R}$ are vectors of a dimensionless Bravais lattice with a unit period, $\mathbf{q} = \mathbf{k}a_0$ is a dimensionless wave vector (normalized by lattice constant a_0, $\mathbf{k}$ is the wave vector), and $\mathcal{H}_{\mathbf{q}}$ and $\mathcal{S}_{\mathbf{q}}$ are the TB Hamiltonian and overlap matrix. We formally describe the structure of $\mathcal{S}$ and $\mathcal{H}$ using the Slater-Koster approach as follows:

$$\mathcal{H}_{\mathbf{q}} = \sum_{i,j} \left((-1)^{(j-1)}\varepsilon_s\delta_{ij} + t_{ij}^{(2)}\right)(a_i^+ a_j + b_i^+ b_j) + \sum_{i,j}^{\lambda=1,3} t_{ij}^{(\lambda)} a_i^+ b_j + \text{H.c.};$$

$$\mathcal{S}_{\mathbf{q}} = \sum_{i,j} \left(\delta_{ij} + s_{ij}^{(2)}\right)(a_i^+ a_i + b_i^+ b_i) + \sum_{i,j}^{\lambda=1,3} s_{ij}^{(\lambda)} a_i^+ b_j + \text{H.c.};$$

$$s_{11}^{(\lambda)} = s_{22}^{(\lambda)} = f_1^{(\lambda)}S_1^{(\lambda)}; \quad s_{12}^{(\lambda=1,3)} = f_2^{(\lambda)}S_2^{(\lambda)}; \quad s_{21}^{(\lambda=1,3)} = f_3^{(\lambda)}S_2^{(\lambda)}; \quad s_{12}^{(2)} = s_{21}^{(2)*} = f_2^{(2)}S_2^{(2)};$$

$$t_{11}^{(\lambda)} = f_1^{(\lambda)}P_{1+}^{(\lambda)}; \quad t_{22}^{(\lambda)} = f_1^{(\lambda)}P_{1-}^{(\lambda)}; \quad t_{12}^{(\lambda=1,3)} = f_2^{(\lambda)}P_2^{(\lambda)}; \quad t_{21}^{(\lambda=1,3)} = f_3^{(\lambda)}P_2^{(\lambda)}; \quad t_{12}^{(2)} = t_{21}^{(2)*} = f_2^{(2)}P_2^{(2)};$$

$$S_{n=1,2}^{(\lambda)} = \alpha^2\left(3S_{dd\sigma}^{(\lambda)} + 4S_{dd\pi}^{(\lambda)} + S_{dd\delta}^{(\lambda)}\right) - 4\beta^2\left[(-1)^{\lambda\cdot(n-1)}\zeta^2\left(S_{dd\delta}^{(\lambda)} - (-1)^n S_{dd\pi}^{(\lambda)}\right) + (-1)^{\lambda\cdot n}\eta^2\left(S_{pp\sigma}^{(\lambda)} - (-1)^n S_{pp\pi}^{(\lambda)}\right)\right];$$

$$P_{1\pm}^{(\lambda)} = \sum_{s=0,1} (\pm 2)^s\alpha^2\left(3V_{dd\sigma}^{(s,\lambda)} + 4V_{dd\pi}^{(s,\lambda)} + V_{dd\delta}^{(s,\lambda)}\right) + 4(\mp 1)^s\beta^2\left[\zeta^2\left(V_{dd\delta}^{(s,\lambda)} + V_{dd\pi}^{(s,\lambda)}\right) + (-1)^\lambda\eta^2\left(V_{pp\sigma}^{(s,\lambda)} + V_{pp\pi}^{(s,\lambda)}\right)\right];$$

$$P_2^{(\lambda)} = \alpha^2\left(3V_{dd\sigma}^{(0,\lambda)} - 4V_{dd\pi}^{(0,\lambda)} + V_{dd\delta}^{(0,\lambda)}\right) - 4\beta^2\left[(-1)^\lambda\zeta^2\left(V_{dd\delta}^{(0,\lambda)} - V_{dd\pi}^{(0,\lambda)}\right) + \eta^2\left(V_{pp\sigma}^{(0,\lambda)} - V_{pp\pi}^{(0,\lambda)}\right);\right]$$

$$f_n^{(1)} = \frac{e^{-iq_y}}{4}\left[e^{\frac{3iq_y}{2}}\cos\left(\frac{\sqrt{3}q_x}{2} - \frac{2\pi(n-1)}{3}\right) + \frac{1}{2}\right]; \quad f_n^{(3)} = \frac{e^{-iq_y}}{4}\left[\cos\left(\sqrt{3}q_x + \frac{2\pi(n-1)}{3}\right) + \frac{e^{3iq_y}}{2}\right];$$

$$f_1^{(2)} = \frac{1}{4}\left(2\cos\frac{\sqrt{3}q_x}{2}\cos\frac{3q_y}{2} + \cos\sqrt{3}q_x\right); \quad f_2^{(2)} = \frac{1}{4}\left(\cos\sqrt{3}q_x - \cos\frac{\sqrt{3}q_x}{2}\cos\frac{3q_y}{2} - i\sqrt{3}\sin\frac{\sqrt{3}q_x}{2}\sin\frac{3q_y}{2}\right). \tag{3}$$

Here $a_{i=1,2}^{(+)}$ and $b_{i=1,2}^{(+)}$ are projection operators onto $A_{1,2}$ and $B_{1,2}$ components of the four spinor in Eq. (1); $t_{i,j}^{(\lambda)}$ and $s_{i,j}^{(\lambda)}$ are the hopping and overlap parameter coupling i and j orbitals: neighbor rank λ identifies the coordination circle for the sites involved in a hop ($\lambda = 1$ corresponds to nearest-neighbour hop between different sublattice sites denoted as AB1 in Fig. 2(a), $\lambda = 2$ is the shortest intrasublattice hop denoted as AA1, $\lambda = 3$ is the second-neighbour intersublattice hop AB2, etc.). The first term in $\mathcal{H}$ describes on-site splitting of the orbitals due to SOC and accounts for the six shortest ($\lambda = 2$) intrasublattice (A-A and B-B) hops. The second term describes three A-B and B-A hops, taking into account both closest ($\lambda = 1$) and next-neighbour ($\lambda = 3$) processes. An advantage of the proposed basis (1) is that each of the hopping elements is factorized into k-dependent functions $f_n^{(\lambda)}(\mathbf{q})$ and fitting parameters $P_n^{(\lambda)}$. The latter can be formally related to Slater-Koster (SK) parameters [48] for d and p orbitals $V_\alpha^{(s,\lambda)}$ of two types indicated by index $s = 0, 1$. Those marked by $s = 0$ correspond to two-center SK integrals of the spin-independent time-reversal-symmetric part of the one-electron Hamiltonian of the crystal; parameters with $s = 1$ are related to the time-reversal symmetry breaking by ferromagnetic ordering brought up by SOC. Similarly, the elements

of the overlap matrix $\mathcal{S}$ are expressed through two-center SK integrals but without any SOC contribution. Further details on hopping parameters are given in the Supplemental Material [47], including a discussion of longer hops ($\lambda = 4, 5$).

The fitted values of TB parameters are listed in Table I and graphically represented in Fig. 2(b). Figure 2(c) displays a direct comparison between the lowest spin-polarized conduction bands quadruplets computed using DFT (solid lines) and our TB model (dashed lines). While Fig. 2 shows an already very accurate fit for the lower band, the extended TB model

TABLE I. The values used for the parametrization of the tight-binding model. The rows are for neighbor rank λ. The precision to which each value is given is based on sensitivity of the discrepancy between the TB and DFT spectra with respect to variation of the corresponding parameter.

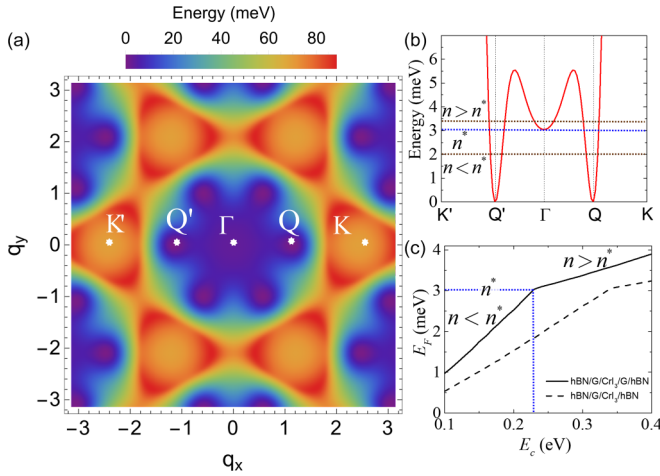|	$P_{1+}^{(\lambda)}$ (meV)	$P_{1-}^{(\lambda)}$ (meV)	$P_2^{(\lambda)}$ (meV)	$S_1^{(\lambda)}$	$S_2^{(\lambda)}$
$\lambda = 1$	122	31	−43	−2.88	0.91
$\lambda = 2$	−54	−151	−35	0.53	0.34
$\lambda = 3$	213	181	−243	−0.13	−0.20
On-site SOC ε_s				38 meV	

FIG. 3. Lower conduction band filling of CrI$_3$ monolayer. (a) The energy profile map of the lower conduction band; the band edge is at six Q,Q' points. (b) Lower energy band profile along the $K' - \Gamma - K$ path. Below critical value of the doping n^* only the Q-point minima are filled, at the doping $n > n^*$ the filling of the minima at Γ begins. (c) The Fermi level relative to the band edge as a function of G-CrI$_3$ band offset for hBN/G/CrI$_3$/G/hBN (solid line) and hBN/G/CrI$_3$/hBN (dashed line) stacks. The regions corresponding to below critical and above critical value n^* are indicated.

accounting for longer hops achieves a better agreement for other bands, too [47]. A remarkable feature of the identified parameters is the relevance of hops beyond nearest neighbor, in particular, the large magnitude of overlap parameters $S_{1,2}^{(1)}$. On the one hand a large intersite overlap and the nonorthogonality of the basis (1) would make it difficult to use the proposed TB for many-body calculations. On the other hand, it points to that the hops are mediated by the halogens, which could be used to formulate a TB model with a basis expanded by, e.g., p orbitals of halogens. This extension of the TB model we leave for future studies and, here, simply use the accurate semianalytical description of the lowest conduction band in the quadruplet to analyze the charge transfer in CrX_3/G heterostructures.

III. GRAPHENE/CrI$_3$ HETEROSTRUCTURE

In Fig. 2(c), the lowest among the conduction band quadruplet of CrI$_3$ is quite flat. The details of the dispersion of this lowest band are elaborated using the semianalytical description enabled by TB Hamiltonian (3) and are shown in Fig. 3(a). This band features six edge points Q, located approximately halfway along a $\Gamma - K$ path: here we identify three Q and Q' pairs related by time inversion of reciprocal space. The dispersion at the band minima is parabolic with slightly anisotropic effective masses $m_1 = 0.54 m_0$, $m_2 = 0.58 m_0$, m_0 being the free electron mass. An additional minimum at the Γ point is located ≈ 3 meV above the band edge with an isotropic effective mass exceeding $10 m_0$ producing a sufficiently high capacity of electron states for pinning the Fermi level in CrI$_3$ at high doping densities $n > n^*$. From this we conclude that in terms of doping the essential bandwidth of the CrI$_3$ monolayer is ≈ 3 meV, so that the charge transfer into it from the environment such as graphene (Fig. 1)
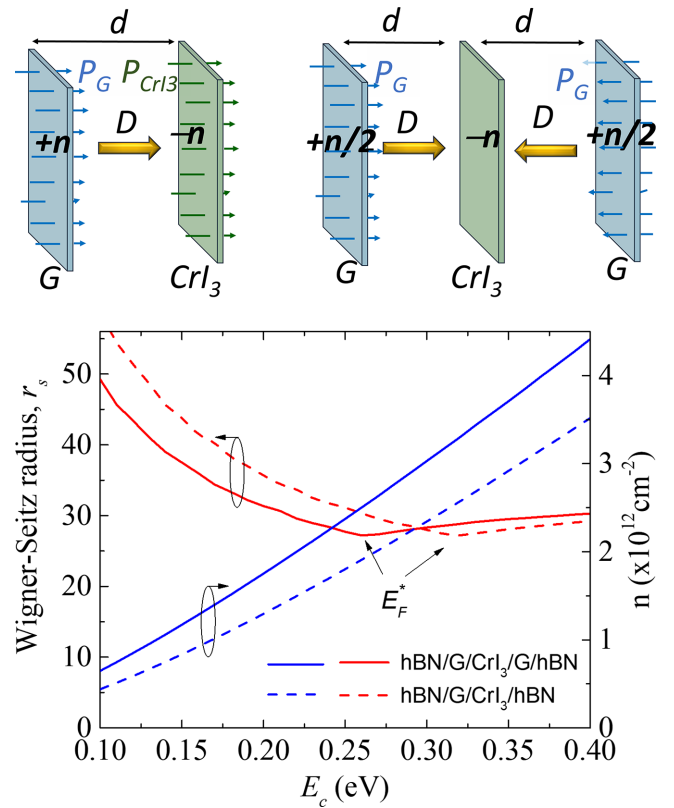

FIG. 4. Charge transfer in CrI$_3$-graphene stacks. Top: Sketches illustrating charge transfer in a CrI$_3$/G stack (left) and G/CrI$_3$/G (right). The transferred sheet density n creates a positive charge at graphene and negative charge at CrI$_3$, producing a displacement field D and intralayer polarizations [see Eqs. (4) and (5)]. Bottom: transferred carrier density, n (red lines, r.h.s. axis) and Wigner-Seitz radius, r_s (blue lines, l.h.s. axis) as functions of the band offset, E_c. Solid lines correspond to hBN-encapsulated trilayer hBN/G/CrI$_3$/G/hBN, dashed lines correspond to hBN/G/CrI$_3$/hBN, and E_F^* corresponds to the Fermi level reaching the Γ valley edge.

is determined by the interplay between the single-particle band offset, E_c, between the above-mentioned CrI$_3$ band and graphene Dirac point, electrostatics (classical capacitance), and Fermi level of holes in graphene (quantum capacitance contribution). The band edge profile along the $K' - \Gamma - K$ direction is shown in Fig 3(c).

It has been reported based on first-principles calculations that the electron affinity of the CrI$_3$ monolayer exceeds the work function of undoped graphene by $E_c \approx 0.2-0.4$ eV, suggesting a charge transfer between the layers in G/CrI$_3$ heterostructures [33,36]. A charge transfer of up to $\sim 10^{13}$ cm^{-2}, also electrically tunable, has been observed experimentally for graphene-CrX_3 interfaces, $X =$ I, Cl, Br [10,32,49–51]. While one reason for such transfer could be related to defects in the crystal, suggestions have been made that the observed graphene p doping is associated with electron transfer into a CrX_3 conduction band. Using the structure of the lowest conduction band of CrI$_3$ obtained by our modeling, we calculate the charge transfer for G/CrI$_3$/G and G/CrI$_3$ stacks shown schematically in Fig. 4.

For the G/CrI$_3$ stack, the corresponding capacitor model is sketched in Fig. 4 (left). Here a difference V between the on-layer potential energies of graphene and CrI$_3$ layers can be expressed as

$$V = \frac{ed}{\varepsilon_0}\left(en - \frac{P_G}{2} - \frac{P_{CrI_3}}{2}\right); \quad P = (\varepsilon - 1)\left(\frac{en}{2} - P\right), \quad (4)$$

where n is the sheet density of transferred carriers, d is the distance between the middle of the layers (i.e., carbon and chromium planes), ε_{G,CrI_3} are the out-of-plane dielectric susceptibilities of graphene and CrI$_3$ monolayers, n is the mobile charge sheet densities in the monolayers, P_{G,CrI_3} denotes polarizations of the corresponding layers [see Fig. 4(a)]. In the expression for V [Eq. (4)] the first term in brackets is due to displacement field produced by the transferred charge in the layers, while two other terms take into account the layer's dielectric polarisations, as sketched in Fig. 4. Here we note that the out-of-plane polarization of each layer is caused by the other layer, which is reflected by a factor of 1/2 in the expression for P in [Eq. (4)] (because the dielectric polarization of a monolayer is not affected by displacement field generated by transferred charge of itself due to mirror reflection symmetry in each monolayer plane [52]).

For the case of CrI$_3$ sandwiched between two graphene layers, the corresponding capacitor model is sketched in Fig. 4 (right). In this case, the CrI$_3$ layer in the middle is not polarized, due to the symmetry of the structure. The expression for the electrostatic energy difference between a graphene and CrI$_3$ monolayer takes the form

$$V = \frac{ed}{\varepsilon_0}\left(en - \frac{P_G}{2}\right); \quad P_G = (\varepsilon_G - 1)\left(\frac{en}{2} - P_G\right), \quad (5)$$

where n is determined as electron density in CrI$_3$ (therefore, both graphene layers are doped with $n/2$ holes).

The carrier density in CrI$_3$, n, and the position of the Fermi level for both one- and two-graphene cases can be obtained from the overall charge neutrality of a stack, combined with Eqs. (4) and (5):

$$n = \frac{\varepsilon_0 \alpha V}{e^2 d} = N_G \int_0^{E_c - V - E_F} \frac{2E\,dE}{\pi v^2 \hbar^2} = \int_0^{E_F} \rho(E)\,dE,$$

$$\alpha_{G/CrI_3} = \frac{4\varepsilon_G \varepsilon_{CrI_3}}{2\varepsilon_G \varepsilon_{CrI_3} + \varepsilon_{CrI_3} + \varepsilon_G}; \quad \alpha_{G/CrI_3/G} = \frac{8\varepsilon_G}{3\varepsilon_G + 1}, \quad (6)$$

where ρ is the density of states of the CrI$_3$ monolayer, and $N_G = 1, 2$ indicates the number of graphene layers in the stack. For numerical simulations we use $\varepsilon_G = 2.6$ [52], $\varepsilon_{CrI_3} = 4$ [19], and $d = 0.5$ nm [53]. The resulting dependence of E_F and n on the G/CrI$_3$ band offset, E_c, is shown in Figs. 3(c) and 4, respectively. The analyzed interval of E_c covers the values suggested in Ref. [36]. We note that density n^* corresponds to $E_c^* \approx 0.2$ eV.

To assess how heavy are the electrons populating the CrI$_3$ band, we compute the Wigner-Seitz radius for the analyzed interval of doping [54–56], Fig. 4. Unlike electrostatics determining the charge transfer discussed above, the Coulomb interaction within the layer largely depends on the in-plane polarization properties of the media and encapsulation of the

stacks, in particular hBN-encapsulated structures. For a bulk hexagonal BN encapsulation $\varepsilon_{hBN} = \sqrt{\varepsilon_{hBN}^{\|c} \varepsilon_{hBN}^{\perp c}}$, where we take $\varepsilon_{hBN}^{\|c} = 3.5$, $\varepsilon_{hBN}^{\perp c} = 6.9$ for the dielectric constant parallel and perpendicular to c axes, respectively [57–59], resulting in $\varepsilon_{hBN} = 4.9$. Then, we note that, due to spin + valley degeneracy, number of graphene layers (top and bottom), and steep dispersion of Dirac holes, screening of Coulomb repulsion of heavy electrons in the magnetic layer by graphene is inefficient (in particular, because the average distance between the electrons in CrI$_3$ is much smaller than the Fermi wavelength of holes in graphene). Therefore, we determine the Wigner-Seits radius as

$$r_s = \frac{e^2 \sqrt{\pi n}}{4\pi \varepsilon_{hBN} \varepsilon_0 E_F},$$

and plot its computed values in Fig. 4. For the range of G/CrX$_3$ band offsets suggested in the recent literature, the resulting r_s values fall in the range $25 < r_s < 35$, which indicate that heavy electrons in CrI$_3$ would be strongly correlated. We note that for $n < n^*$, apart from r_s, the valley degeneracy (six Q points) significantly impacts the importance of many-body effects. However, this impact does not simply reduce to a modification of r_s; it depends on the specific effects being considered [60]. As a result, here, we get a type-II semiconductor system hosting light highly mobile holes in graphene(s) compensating heavy electrons in CrI$_3$, with a Wigner-Seitz radius almost in the range of Wigner crystallization conditions.

IV. DISCUSSION

Based on the data presented in Fig. 4 we note that the charge transfer to the CrI$_3$ monolayer band and the corresponding p doping of graphene appears to be several times lower than the charge transfer evidenced by $\sim(5-10) \times 10^{12}$ cm^{-2} graphene doping (both monolayer and bilayer) experimentally observed in one-sided graphene on thick CrI$_3$ heterostructures [10,32]. This discrepancy can be attributed to either a contribution of defects producing in-gap states [61], or to a substantial broadening of the conduction band in
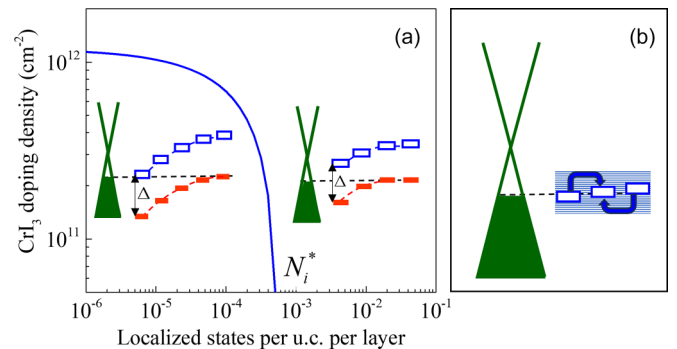

FIG. 5. Sketch of a charge transfer between graphene and bulk CrI$_3$. (a) In-gap defects ($\Delta \sim 0.5$ eV) in multiple CrI$_3$ layers reduce conduction band filling, completely quenching it when the number of localized states per unit cell in each monolayer is $N_i > N_i^*$, as computed for $E_c = 0.2$ eV. (b) CrI$_3$ conduction band broadening by the interlayer hybridization could also shrink the bandgap for a bulk material, hence, increasing a charge transfer from graphene.

multilayer CrI_3 by the interlayer hybridization (thus shrinking the bandgap, similar to what has been found in InSe [62,63]).

We illustrate the influence of in-gap states in Fig. 5(a) by analyzing a simultaneous filling of in-gap and band states for G/CrI_3 offset $E_c = 0.2$ eV and note that $N_i^* \sim 0.5 \times 10^{-3}$ defects per CrI_3 unit cell per layer would quench the conduction band occupancy by electron transfer into several CrI_3 layers near its surface. From this point of view, the suggested heterostructures based on monolayer CrI_3 would reduce the role of in-gap defects. Moreover, the graphene-encapsulated CrI_3 monolayer ($G/CrI_3/G$) would be an even more promising system for bringing up the above-discussed strongly correlated heavy electrons.

As to the alternative option, related to the interlayer hybridization of CrI_3 band states, its careful quantitative description would require an extension of the TB model (3) onto multilayer structures. For developing such an extension it is worth noting a dominant role of the next-unit-cell hops between chromium orbital highlighted in Fig. 2(b). The latter feature of the developed TB model can be attributed to involving halogen orbitals as intermediate states in the hopping process. At the same time halogen orbitals should be accounted for in the interlayer hybridization as the halogen ions are located in the outer sublayers of the 2D crystal. This suggests an alternative formulation of a TB model for CrX_3 where the minimum number of Cr orbitals coupled by several neighbor hops will be superseded by a combination of Cr and halogen orbitals with only Cr-halogen and nearest-neighbor halogen-halogen hops (both within and between the layers).

ACKNOWLEDGMENTS

[1] H. Kurebayashi, J. H. Garcia, S. Khan, J. Sinova, and S. Roche, Magnetism, symmetry and spin transport in van der Waals layered systems, Nat. Rev. Phys. **4**, 150 (2022).

[2] B. Huang, M. A. McGuire, A. F. May, D. Xiao, P. Jarillo-Herrero, and X. Xu, Emergent phenomena and proximity effects in two-dimensional magnets and heterostructures, Nat. Mater. **19**, 1276 (2020).

[3] D. Soriano, M. I. Katsnelson, and J. Fernández-Rossier, Magnetic two-dimensional chromium trihalides: A theoretical perspective, Nano Lett. **20**, 6225 (2020).

[4] K. S. Burch, D. Mandrus, and J.-G. Park, Magnetism in two-dimensional van der Waals materials, Nature (London) **563**, 47 (2018).

[5] Q. H. Wang, A. Bedoya-Pinto, M. Blei, A. H. Dismukes, A. Hamo, S. Jenkins, M. Koperski, Y. Liu, Q.-C. Sun, E. J. Telford, H. H. Kim, M. Augustin, U. Vool, J.-X. Yin, L. H. Li, A. Falin, C. R. Dean, F. Casanova, R. F. L. Evans, M. Chshiev, A. Mishchenko, C. Petrovic, R. He, L. Zhao, A. W. Tsen, B. D. Gerardot, M. Brotons-Gisbert, Z. Guguchia, X. Roy, S. Tongay, Z. Wang, M. Z. Hasan, J. Wrachtrup, A. Yacoby, A. Fert, S. Parkin, K. S. Novoselov, P. Dai, L. Balicas, and E. J. G. Santos, The magnetic genome of two-dimensional van der Waals materials, ACS Nano **16**, 6960 (2022).

[6] M. Gibertini, M. Koperski, A. F. Morpurgo, and K. S. Novoselov, Magnetic 2D materials and heterostructures, Nat. Nanotechnol. **14**, 408 (2019).

[7] M. A. McGuire, H. Dixit, V. R. Cooper, and B. C. Sales, Coupling of crystal structure and magnetism in the layered, ferromagnetic insulator CrI_3, Chem. Mater. **27**, 612 (2015).

[8] M.-C. Wang, C.-C. Huang, C.-H. Cheung, C.-Y. Chen, S. G. Tan, T.-W. Huang, Y. Zhao, Y. Zhao, G. Wu, Y.-P. Feng, H.-C. Wu, and C.-R. Chang, Prospects and opportunities of 2D van der Waals magnetic systems, Annalen der Physik **532**, 1900452 (2020).

[9] L. Thiel, Z. Wang, M. A. Tschudin, D. Rohner, I. Gutiérrez-Lezama, N. Ubrig, M. Gibertini, E. Giannini, A. F. Morpurgo, and P. Maletinsky, Probing magnetism in 2D materials at the nanoscale with single-spin microscopy, Science **364**, 973 (2019).

[10] G. Tenasini, D. Soler-Delgado, Z. Wang, F. Yao, D. Dumcenco, E. Giannini, K. Watanabe, T. Taniguchi, C. Moulsdale, A. Garcia-Ruiz, V. I. Fal'ko, I. Gutiérrez-Lezama, and A. F. Morpurgo, Band gap opening in bilayer graphene-$CrCl_3/CrBr_3/CrI_3$ van der Waals interfaces, Nano Lett. **22**, 6760 (2022).

[11] F. Yao, V. Multian, Z. Wang, N. Ubrig, J. Teyssier, F. Wu, E. Giannini, M. Gibertini, I. Gutiérrez-Lezama, and A. F. Morpurgo, Multiple antiferromagnetic phases and magnetic anisotropy in exfoliated $CrBr_3$ multilayers, Nat. Commun. **14**, 4969 (2023).

[12] Q. Yang, X. Hu, X. Shen, A. V. Krasheninnikov, Z. Chen, and L. Sun, Enhancing ferromagnetism and tuning electronic properties of CrI_3 monolayers by adsorption of transition-metal atoms, ACS Appl. Mater. Interfaces **13**, 21593 (2021).

[13] X. Lu, R. Fei, and L. Yang, Curie temperature of emerging two-dimensional magnetic structures, Phys. Rev. B **100**, 205409 (2019).

[14] H. Zhu, Y. Gao, Y. Hou, Z. Gui, and L. Huang, Tunable magnetic anisotropy in two-dimensional $CrX_3/AlN(X = I, Br, Cl)$ heterostructures, Phys. Rev. B **106**, 134412 (2022).

[15] D. Staros, G. Hu, J. Tiihonen, R. Nanguneri, J. Krogel, M. C. Bennett, O. Heinonen, P. Ganesh, and B. Rubenstein, A combined first principles study of the structural, magnetic, and phonon properties of monolayer CrI_3, J. Chem. Phys. **156**, 014707 (2022).

[16] S. Acharya, D. Pashov, B. Cunningham, A. N. Rudenko, M. Rösner, M. Grüning, M. van Schilfgaarde, and M. I. Katsnelson, Electronic structure of chromium trihalides beyond density functional theory, Phys. Rev. B **104**, 155109 (2021).

[17] Y. O. Kvashnin, A. Bergman, A. I. Lichtenstein, and M. I. Katsnelson, Relativistic exchange interactions in CrX_3 (X = Cl, Br, I) monolayers, Phys. Rev. B **102**, 115162 (2020).

[18] M. Wu, Z. Li, and S. G. Louie, Optical and magneto-optical properties of ferromagnetic monolayer $CrBr_3$: A first-principles

GW and *GW* plus Bethe-Salpeter equation study, Phys. Rev. Mater. **6**, 014008 (2022).

[19] M. Wu, Z. Li, T. Cao, and S. G. Louie, Physical origin of giant excitonic and magneto-optical responses in two-dimensional ferromagnetic insulators, Nat. Commun. **10**, 2371 (2019).

[20] M. Akram, H. LaBollita, D. Dey, J. Kapeghian, O. Erten, and A. S. Botana, Moiré skyrmions and chiral magnetic phases in twisted Cr*X*₃ (X = I, Br, and Cl) bilayers, Nano Lett. **21**, 6633 (2021).

[21] R. A. Beck, L. Lu, P. V. Sushko, X. Xu, and X. Li, Defect-induced magnetic skyrmion in a two-dimensional chromium triiodide monolayer, JACS Au **1**, 1362 (2021).

[22] A. O. Fumega and J. L. Lado, Moiré-driven multiferroic order in twisted CrCl₃, CrBr₃ and CrI₃ bilayers, 2D Mater. **10**, 025026 (2023).

[23] H. Xie, X. Luo, G. Ye, Z. Ye, H. Ge, S. H. Sung, E. Rennich, S. Yan, Y. Fu, S. Tian, H. Lei, R. Hovden, K. Sun, R. He, and L. Zhao, Twist engineering of the two-dimensional magnetism in double bilayer chromium triiodide homostructures, Nat. Phys. **18**, 30 (2022).

[24] K. Dolui, M. D. Petrović, K. Zollner, P. Plecháč, J. Fabian, and B. K. Nikolić, Proximity spin–orbit torque on a two-dimensional magnet within van der Waals heterostructure: Current-driven antiferromagnet-to-ferromagnet reversible nonequilibrium phase transition in bilayer CrI₃, Nano Lett. **20**, 2288 (2020).

[25] K. W. Song and V. I. Fal'ko, Superexchange and spin-orbit coupling in monolayer and bilayer chromium trihalides, Phys. Rev. B **106**, 245111 (2022).

[26] K. W. Song, Interlayer superexchange in bilayer chromium trihalides, Phys. Rev. B **107**, 245133 (2023).

[27] D. Soriano, C. Cardoso, and J. Fernández-Rossier, Interplay between interlayer exchange and stacking in CrI₃ bilayers, Solid State Commun. **299**, 113662 (2019).

[28] R. A. Beck, S. Sun, X. Xu, D. R. Gamelin, T. Cao, and X. Li, Understanding external pressure effects and interlayer orbital exchange pathways in the two-dimensional magnet-chromium triiodide, J. Phys. Chem. C **126**, 19327 (2022).

[29] A. Ghosh, D. Singh, T. Aramaki, Q. Mu, V. Borisov, Y. Kvashnin, G. Haider, M. Jonak, D. Chareev, S. A. Medvedev, R. Klingeler, M. Mito, E. H. Abdul-Hafidh, J. Vejpravova, M. Kalbàč, R. Ahuja, O. Eriksson, and M. Abde-Hafiez, Exotic magnetic and electronic properties of layered CrI₃ single crystals under high pressure, Phys. Rev. B **105**, L081104 (2022).

[30] D. R. Klein, D. MacNeill, Q. Song, D. T. Larson, S. Fang, M. Xu, R. A. Ribeiro, P. C. Canfield, E. Kaxiras, R. Comin, and P. Jarillo-Herrero, Enhancement of interlayer exchange in an ultrathin two-dimensional magnet, Nat. Phys. **15**, 1255 (2019).

[31] L. Webster and J.-A. Yan, Strain-tunable magnetic anisotropy in monolayer CrCl₃, CrBr₃, and CrI₃, Phys. Rev. B **98**, 144411 (2018).

[32] C.-C. Tseng, T. Song, Q. Jiang, Z. Lin, C. Wang, J. Suh, K. Watanabe, T. Taniguchi, M. A. McGuire, D. Xiao, J.-H. Chu, D. H. Cobden, X. Xu, and M. Yankowitz, Gate-tunable proximity effects in graphene on layered magnetic insulators, Nano Lett. **22**, 8495 (2022).

[33] C. Cardoso, A. T. Costa, A. H. MacDonald, and J. Fernández-Rossier, Strong magnetic proximity effect in van der Waals heterostructures driven by direct hybridization, Phys. Rev. B **108**, 184423 (2023).

[34] D. Zhong, K. L. Seyler, X. Linpeng, N. P. Wilson, T. Taniguchi, K. Watanabe, M. A. McGuire, K.-M. C. Fu, D. Xiao, W. Yao, and X. Xu, Layer-resolved magnetic proximity effect in van der Waals heterostructures, Nat. Nanotechnol. **15**, 187 (2020).

[35] Y. Wu, Q. Cui, M. Zhu, X. Liu, Y. Wang, J. Zhang, X. Zheng, J. Shen, P. Cui, H. Yang, and S. Wang, Magnetic exchange field modulation of quantum Hall ferromagnetism in 2D van der Waals CrCl₃/graphene heterostructures, ACS Appl. Mater. Interfaces **13**, 10656 (2021).

[36] J. Zhang, B. Zhao, T. Zhou, Y. Xue, C. Ma, and Z. Yang, Strong magnetization and chern insulators in compressed graphene/CrI₃ van der Waals heterostructures, Phys. Rev. B **97**, 085401 (2018).

[37] Z. Wu, J. Yu, and S. Yuan, Strain-tunable magnetic and electronic properties of monolayer CrI₃, Phys. Chem. Chem. Phys. **21**, 7750 (2019).

[38] A. B. Georgescu, A. J. Millis, and J. M. Rondinelli, Trigonal symmetry breaking and its electronic effects in the two-dimensional dihalides *MX*₂ and trihalides *MX*₃, Phys. Rev. B **105**, 245153 (2022).

[39] M. Grzeszczyk, S. Acharya, D. Pashov, Z. Chen, K. Vaklinova, M. van Schilfgaarde, K. Watanabe, T. Taniguchi, K. S. Novoselov, M. I. Katsnelson, and M. Koperski, Strongly correlated exciton-magnetization system for optical spin pumping in CrBr₃ and CrI₃, Adv. Mater. **35**, 2209513 (2023).

[40] N. Ubrig, Z. Wang, J. Teyssier, T. Taniguchi, K. Watanabe, E. Giannini, A. F. Morpurgo, and M. Gibertini, Low-temperature monoclinic layer stacking in atomically thin CrI₃ crystals, 2D Mater. **7**, 015007 (2020).

[41] Z. Liu, Y. Guo, Z. Chen, T. Gong, Y. Li, Y. Niu, Y. Cheng, H. Lu, L. Deng, and B. Peng, Observation of intrinsic crystal phase in bare few-layer CrI₃, Nanophotonics **11**, 4409 (2022).

[42] T. Li, S. Jiang, N. Sivadas, Z. Wang, Y. Xu, D. Weber, J. E. Goldberger, K. Watanabe, T. Taniguchi, C. J. Fennie, K. Fai Mak, and J. Shan, Pressure-controlled interlayer magnetism in atomically thin CrI₃, Nat. Mater. **18**, 1303 (2019).

[43] S. Djurdjić-Mijin, A. Šolajić, J. Pešić, M. Šćepanović, Y. Liu, A. Baum, C. Petrovic, N. Lazarević, and Z. V. Popović, Lattice dynamics and phase transition in CrI₃ single crystals, Phys. Rev. B **98**, 104307 (2018).

[44] P. Giannozzi, S. Baroni, N. Bonini, M. Calandra, R. Car, C. Cavazzoni, D. Ceresoli, G. L. Chiarotti, M. Cococcioni, I. Dabo, A. D. Corso, S. de Gironcoli, S. Fabris, G. Fratesi, R. Gebauer, U. Gerstmann, C. Gougoussis, A. Kokalj, M. Lazzeri, L. Martin-Samos, N. Marzari, F. Mauri, R. Mazzarello, S. Paolini, A. Pasquarello, L. Paulatto, C. Sbraccia, S. Scandolo, G. Sclauzero, A. P. Seitsonen, A. Smogunov, P. Umari, and R. M. Wentzcovitch, QUANTUM ESPRESSO: A modular and open-source software project for quantum simulations of materials, J. Phys.: Condens. Matter **21**, 395502 (2009).

[45] P. Giannozzi, Jr., O. Andreussi, T. Brumme, O. Bunau, M. B. Nardelli, M. Calandra, R. Car, C. Cavazzoni, D. Ceresoli, M. Cococcioni, N. Colonna, I. Carnimeo, A. D. Corso, S. de Gironcoli, P. Delugas, R. A. DiStasio, A. Ferretti, A. Floris, G. Fratesi, G. Fugallo, R. Gebauer, U. Gerstmann, F. Giustino, T. Gorni, J. Jia, M. Kawamura, H.-Y. Ko, A. Kokalj, E. Küçükbenli, M. Lazzeri, M. Marsili, N. Marzari, F. Mauri, N. L. Nguyen, H.-V. Nguyen, A. O. de-la Roza, L. Paulatto, S. Poncé, D. Rocca, R. Sabatini, B. Santra, M. Schlipf, A. P. Seitsonen, A. Smogunov, I. Timrov, T. Thonhauser, P. Umari, N. Vast, X. Wu,

and S. Baroni, Advanced capabilities for materials modelling with QUANTUM ESPRESSO, J. Phys.: Condens. Matter **29**, 465901 (2017).

[46] J. P. Perdew, K. Burke, and M. Ernzerhof, Generalized gradient approximation made simple, Phys. Rev. Lett. **77**, 3865 (1996).

[47] See Supplemental Material at http://link.aps.org/supplemental/10.1103/PhysRevMaterials.8.074007 for details of tight-binding model parametrization and effect of spin-orbit coupling.

[48] J. C. Slater and G. F. Koster, Simplified LCAO method for the periodic potential problem, Phys. Rev. **94**, 1498 (1954).

[49] Y. Zhang, J. Liu, R. Deng, X. Shi, H. Tang, H. Chen, and H. Yuan, Electronic structure, magnetoresistance and spin filtering in graphene|2 monolayer-CrI₃|graphene van der Waals magnetic tunnel junctions, RSC Adv. **12**, 28533 (2022).

[50] S. Jiang, L. Li, Z. Wang, K. F. Mak, and J. Shan, Controlling magnetism in 2D CrI₃ by electrostatic doping, Nat. Nanotechnol. **13**, 549 (2018).

[51] S. Jiang, L. Li, Z. Wang, J. Shan, and K. F. Mak, Spin tunnel field-effect transistors based on two-dimensional van der Waals heterostructures, Nature Electronics **2**, 159 (2019).

[52] S. Slizovskiy, A. Garcia-Ruiz, A. I. Berdyugin, N. Xin, T. Taniguchi, K. Watanabe, A. K. Geim, N. D. Drummond, and V. I. Fal'ko, Out-of-plane dielectric susceptibility of graphene in twistronic and bernal bilayers, Nano Lett. **21**, 6678 (2021).

[53] M. U. Farooq and J. Hong, Switchable valley splitting by external electric field effect in graphene/CrI₃ heterostructures, npj 2D Mater. Appl. **3**, 3 (2019).

[54] E. Y. Andrei, G. Deville, D. C. Glattli, F. I. B. Williams, E. Paris, and B. Etienne, Observation of a magnetically induced wigner solid, Phys. Rev. Lett. **60**, 2765 (1988).

[55] L. O. Wagner and P. Gori-Giorgi, Electron avoidance: A nonlocal radius for strong correlation, Phys. Rev. A **90**, 052512 (2014).

[56] S. T. Chui, M. Huang, Z. Wu, and N. Wang, Giant enhanced stability of the quantum electron solid from a weakened electron-electron interaction in double-layer MoS₂, Phys. Rev. B **109**, 165412 (2024).

[57] A. Laturia, M. L. Van de Put, and W. G. Vandenberghe, Dielectric properties of hexagonal boron nitride and transition metal dichalcogenides: From monolayer to bulk, npj 2D Mater. Appl. **2**, 6 (2018).

[58] A. Pierret, D. Mele, H. Graef, J. Palomo, T. Taniguchi, K. Watanabe, Y. Li, B. Toury, C. Journet, P. Steyer, V. Garnier, A. Loiseau, J.-M. Berroir, E. Bocquillon, G. Fève, C. Voisin, E. Baudin, M. Rosticher, and B. Plaçais, Dielectric permittivity, conductivity and breakdown field of hexagonal boron nitride, Mater. Res. Express **9**, 065901 (2022).

[59] N. Ohba, K. Miwa, N. Nagasako, and A. Fukumoto, First-principles study on structural, dielectric, and dynamical properties for three BN polytypes, Phys. Rev. B **63**, 115207 (2001).

[60] S. Das Sarma, E. H. Hwang, and Q. Li, Valley-dependent many-body effects in two-dimensional semiconductors, Phys. Rev. B **80**, 121303(R) (2009).

[61] J. Zhang, Y. Guo, P. Li, J. Wang, S. Zhou, J. Zhao, D. Guo, and D. Zhong, Imaging vacancy defects in single-layer chromium triiodide, J. Phys. Chem. Lett. **12**, 2199 (2021).

[62] S. J. Magorrian, V. Zólyomi, and V. I. Fal'ko, Electronic and optical properties of two-dimensional inse from a dft-parametrized tight-binding model, Phys. Rev. B **94**, 245431 (2016).

[63] D. A. Bandurin, A. V. Tyurnina, G. L. Yu, A. Mishchenko, V. Zólyomi, S. V. Morozov, R. K. Kumar, R. V. Gorbachev, Z. R. Kudrynskyi, S. Pezzini, Z. D. Kovalyuk, U. Zeitler, K. S. Novoselov, A. Patanè, L. Eaves, I. V. Grigorieva, V. I. Fal'ko, A. K. Geim, and Y. Cao, High electron mobility, quantum Hall effect and anomalous optical response in atomically thin inse, Nat. Nanotechnol. **12**, 223 (2017).